Tech Science Press

Analysis of Water Transport inside a Plant Xylem Vessel with Pitted Thickening

Tianyu Xu and Lixiang Zhang*

Faculty of Civil Engineering and Mechanics, Kunming University of Science and Technology, Kunming, 650500, China
*Corresponding Author: Lixiang Zhang. Email: emzhanglx@kmust.edu.cn

Abstract: In this article, computational fluid dynamics (CFD) are used to explore the dynamics of water transport inside the pitted thickening of a plant xylem vessel. A pitted thickening model combined with the Bernoulli equation is used to analyze the influence of various factors (namely, the inner diameter, thickening width, thickening height, thickening spacing, number of laps and adjacent pit axial rotation). The pressure drop and the flow resistance coefficient are the variable parameters for our analysis. The results show that these two parameters are proportional to the thickening height and thickening width, and inversely proportional to the inner diameter, thickening spacing and number of laps. Three different wall thickening structures of the vessel are compared and the pitted thickening vessel is shown to provide the largest structural flow resistance, the annular thickening vessel has the second largest resistance and the helical thickening vessel corresponds to the smallest resistance of the three structures.

1 Introduction

Water plays an important role in the physiological ecology of plants and can directly or indirectly affect various physiological activities during plant growth and development. The mechanism of water transport has always been an active research area [1]. The xylem is the main water transport channel that connects the root system and the canopy. Water passes from the roots to the leaves through the xylem, using the vessels and tracheids distributed throughout the xylem as the transport channels [2,3]. The length of the vessels vary but their inner diameter is generally in the micron scale, which makes it difficult to calculate the water transfer capabilities of each vessel [4,5]. Currently, experimental observation is the main method used [6,7].

To address the deficiencies of experimental observation, some scholars have explored the flow characteristics of a xylem vessel by constructing a xylem vessel model and using the Computational Fluid Dynamics (CFD) method [8]. Roth [9] has established a two-dimensional simplified model of a vessel which analyzed the flow characteristics of the ring thickenings and concluded that water flow characteristics are related to the two closest adjacent thickenings. Schulte [10] has analyzed the water flow characteristics of a 20-hole perforated plate of xylem tube using experiments and simulations. The experimental results showed that the water flow resistance of the perforated plate accounted for 21% of the total water transport resistance and the simulated value was 23%. Ai [11] has simulated the pressure

distribution and velocity distribution of the ladder-shaped perforated plate based on the k-ε model and discovered that the number of holes in the perforated plate is proportional to the total pressure drop. Most of the previous study models are based on analysis of ring thickenings and the perforated plate. Different thickening types appear in an ontogenetic sequence with annular thickening occurring first, followed in order by helical and pitted thickening [12,13], which have different water transport characteristics [14–16]. The influence of pitted thickening on water transport has not been previously studied [17,18]. Therefore, this paper investigates the influence of a pitted thickening vessel on water transport and analyzes the relationship between the resistance for the same parameters with annular or helical thickening [19–22].

In this paper, a pitted thickening structured distribution model is proposed that simulates the effect of xylem vessel thickening on water transport. Combined with Bernoulli's equation, the influence of factors such as the inner diameter, thickening width, thickening height, thickening spacing, number of laps and adjacent pit axial rotation of pitted thickening on the micro-flow inside the vessel were analyzed by varying the flow resistance coefficient to evaluate the effect of xylem vessel thickening on water transport in the vessels during the process of plant growth.

2 Pitted Thickening Vessel Model

2.1 Pitted Thickening Model

The type of secondary wall thickening can be determined by the dimension (diameter) of the vessel and the maturity and growth stage of the plant (ontogeny). Pitted thickening is the most complicated type of thickening of the three possible structures (Fig. 1). The literature contains many descriptions of secondary wall patterns which analyze water transport characteristics of vessels with pitted thickening, but do not provide an exact model. The problem of water transport in a pitted thickening vessel is described in the next section and a possible explanation for the observed behavior is provided.
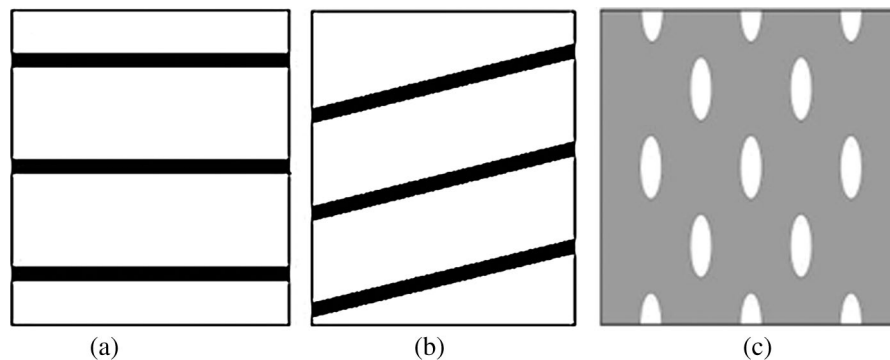

Figure 1: Different secondary wall thickening patterns. (a) Annular thickening; (b) Helical thickening; (c) Pitted thickening

2.2 Different Secondary Wall Thickening Patterns of a Pitted Thickening Model for Different Vessel Types

Several 3D models of plant xylem vessels have been established in the literature [11,15,16] were established to compare the water transport characteristics of different pitted thickening patterns of the xylem, as shown in Fig. 2. Since pitted thickening can have different parameters in different vessels, a model of each vessel is required for analysis. The models contain a flow region with wall thickening patterns of length 150 μm. To avoid effects at the entrance and exit, an extended smooth segment with length 20 μm is added at both ends of the vessel. In Fig. 3, d is the inner diameter, h is the pitted
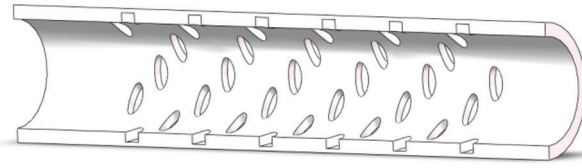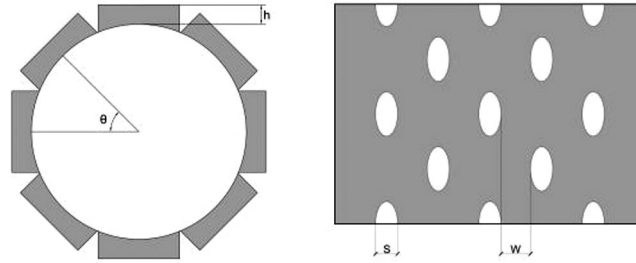
Figure 2: 3D model of pitted thickening

Figure 3: Different parameters of pitted thickening patterns

thickening height, w is the pitted thickening width, s is the pitted thickening spacing, n is the number of laps and θ is the adjacent pit axial rotation.

2.3 Governing Equations

The steady-state conservation equations for mass and momentum in fluid are given as follows [23,24]:

Continuity equation:

$$\frac{\partial u}{\partial x} + \frac{\partial v}{\partial y} + \frac{\partial w}{\partial z} = 0 \tag{1}$$

Momentum equation:

$$\begin{cases} \rho\left(u\frac{\partial u}{\partial x} + v\frac{\partial u}{\partial y} + w\frac{\partial u}{\partial z}\right) = -\frac{\partial P}{\partial x} + \mu\left(\frac{\partial^2 u}{\partial x^2} + \frac{\partial^2 u}{\partial y^2} + \frac{\partial^2 u}{\partial z^2}\right) \\ \rho\left(u\frac{\partial v}{\partial x} + v\frac{\partial v}{\partial y} + w\frac{\partial v}{\partial z}\right) = -\frac{\partial P}{\partial y} + \mu\left(\frac{\partial^2 v}{\partial x^2} + \frac{\partial^2 v}{\partial y^2} + \frac{\partial^2 v}{\partial z^2}\right) \\ \rho\left(u\frac{\partial w}{\partial x} + v\frac{\partial w}{\partial y} + w\frac{\partial w}{\partial z}\right) = -\frac{\partial P}{\partial z} + \mu\left(\frac{\partial^2 w}{\partial x^2} + \frac{\partial^2 w}{\partial y^2} + \frac{\partial^2 w}{\partial z^2}\right) \end{cases} \tag{2}$$

where, u, v and w are the components of the velocity vector along the x, y and z-directions, respectively, ρ is the fluid density, P is the fluid pressure and μ is the dynamic viscosity.

2.4 Bernoulli Equation Model

Fig. 4 provides a schematic cross-sectional view showing the distribution of the pitted thickening model along the inner wall, with the arrow representing the direction of water movement. For the mathematical model, there were several assumptions used for a more reasonable and simpler analysis:

1. The flow is steady and laminar.
2. The fluid is incompressible, Newtonian and viscous.
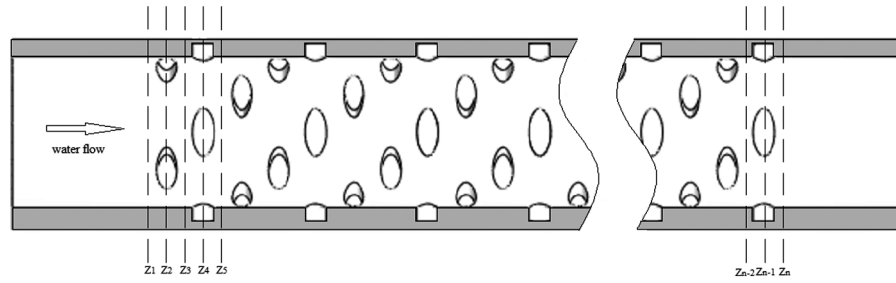3. There is a non-slip velocity.

Figure 4: Schematic of water flow in a pitted thickening vessel

The energy conservation law of liquid flow (the Bernoulli equation) can be used on the model to analyze the fluid flow in the pitted thickening vessel. It is assumed that the flow between arbitrary sections satisfies the Bernoulli equation, which can be written for each section Z_1, Z_2, Z_n from the inlet to the exit as:

$$\frac{P_1}{\rho g} + \frac{V_1^2}{2g} + z_1 = \frac{P_2}{\rho g} + \frac{V_2^2}{2g} + z_2 + \xi_1 \frac{V_2^2}{2g} + \lambda \frac{l_1 V_2^2}{2Dg}$$

$$\frac{P_2}{\rho g} + \frac{V_2^2}{2g} + z_1 = \frac{P_3}{\rho g} + \frac{V_3^2}{2g} + z_3 + \xi_2 \frac{v_3^2}{2g} + \lambda \frac{l_2 V_3^2}{2Dg}$$

$$\cdots\cdots$$
$$\cdots\cdots$$

$$\frac{P_{n-1}}{\rho g} + \frac{V_{n-1}^2}{2g} + z_{n-1} = \frac{P_n}{\rho g} + \frac{V_n^2}{2g} + z_n + \xi_{n-1} \frac{V_n^2}{2g} + \lambda \frac{l_{n-1} V_n^2}{2Dg}$$

(3)

where P_n and V_n are the average pressure and the flow velocity in section n, ρ is the fluid density, g is the acceleration due to gravity, Z_n is the elevation head in the section, ξ_{n-1} is the local loss coefficient between section n-1 to section n, λ is friction factor of the head loss and l_{n-1} is the length between two adjacent sections.

The two sides of the equations in Eq. (3) can be summed in order to obtain:

$$\frac{P_1 - P_n}{\rho g} = z_n - z_1 + \xi_1 \frac{V_2^2}{2g} + \xi_2 \frac{V_3^2}{2g} + \cdots + \xi_{n-1} \frac{V_n^2}{2g} + \lambda \frac{(z_n - z_1)V_n^2}{2Dg}$$

(4)

It is known by the continuity equation that:

$$V_1 A_1 = V_2 A_2 = V_3 A_3 = \cdots = V_n A_n$$

(5)

In Eq. (5), Ai (i = 1, 2..., n) is the flow area of the corresponding section. Substituting Eq. (5) into Eq. (4) gives:

$$\frac{\Delta P}{\rho g} = L + \left[\lambda \left(\frac{A_1}{A_n} \right)^2 \frac{L}{D} + \sum_{i=1}^{n-1} \xi_i \left(\frac{A_1}{A_{i+1}} \right)^2 \right] \frac{V_1^2}{2g}$$

(6)

where:

$$\xi = \lambda \left(\frac{A_1}{A_n} \right)^2 \frac{L}{D} + \sum_{i=1}^{n-1} \xi_i \left(\frac{A_1}{A_{i+1}} \right)^2$$

(7)

Eq. (6) can be simplified to:

$$\frac{\Delta P}{\rho g} = L + \xi \frac{V_1^2}{2g} \tag{8}$$

which can be expressed as:

$$\xi = \frac{2}{V_1^2}\left(\frac{\Delta P}{\rho} - Lg\right) \tag{9a}$$

which can be expressed in terms of the flow rate:

$$\xi = \frac{\pi^2 D^4}{8Q^2}\left(\frac{\Delta P}{\rho} - Lg\right) \tag{9b}$$

In Eqs. (9a) and (9b), ξ is the flow resistance coefficient, $L = z_n$-z_1 is the vessel length (the vertical height) and Q is the average flow rate in the vessel. Obviously, ξ reflects the influence of the pitted thickening inside the vessel and its geometrical characteristics on the flow. A larger value of ξ indicates a larger vessel resistance, and a smaller ξ value indicates a smaller vessel resistance. Eqs. (9a) and (9b) represent the physical and mechanical relationships between the plant vessel geometrical characteristics and the water transport force and driving force, reflecting the mechanism of water transport in plant xylem vessels.

2.5 Initial Condition and Grid

A finite volume method with non-staggered grid technique is used for spatial discretization and a second order implicit scheme is used to discretize time. The SIMPLEC scheme is chosen to achieve a coupling solution for the pressure and velocity equations. The second order scheme is used for the pressure term, and a second order upwind scheme is used for the momentum term. The residuals have convergence criteria of 1×10^{-5} and the maximum number of iterations per time-step is set to 150. The uniform fluid velocity specified at the inlet is 0.3 mm·s^{-1}. For this step, the scale of the mesh is based on the prediction accuracy of the inlet/outlet pressure drop, and so a mesh size independence test is performed with results shown in Tab. 1. The difference in pressure drop between a standard mesh and a fine mesh is 0.21% and so the number of meshes has no effect on the calculation results. Therefore, a standard number of meshes is used. The total number of meshes in a pitted thickening vessel is approximately 0.6 million. The distribution pattern of the pitted thickening wall is shown in Fig. 5. The maximum element size is 1.22×10^{-3} mm and the minimum element size is 2.24×10^{-4} mm. Since the calculation scale can be considered to be small, the simulations are conducted using a PowerCube-S01 cloud cube high performance computing system for parallel computing, based at Kunming University of Science and Technology.

Table 1: Mesh size independence test

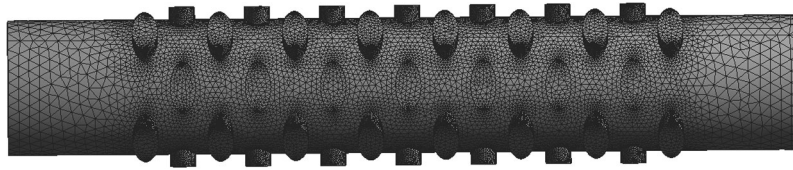|	Mesh number	Pressure drop difference
Very Coarse	114521	–
Coarse	317541	1.18%
Standard	601524	0.46%
Fine	1557854	0.21%

Figure 5: Pitted thickening wall mesh distribution

3 Result and Discussion

3.1 Influence of the Pitted Thickening Patterns

To facilitate a comparative analysis, the model focuses on the pitted thickening patterns and investigates the influence of the inner diameter, thickening width, thickening height, thickening spacing, number of laps and adjacent pit axial rotation on the pressure drop and the flow resistance coefficient of the vessel model.

3.1.1 Influence of the Inner Diameter

For this simulation, the pitted thickening patterns have dimensions of w = 2.3 μm, h = 2.3 μm, s = 4 μm, n = 4 and the axial rotation is 45°. The inner diameter is varied from 20 μm to 30 μm. Tab. 2 shows the influence of the inner diameter on the pressure drop and the flow resistance coefficient.

Table 2: Effect of inner diameter of vessel on the pressure drop and the flow resistance coefficient

Inner diameter of vessel/μm	Pressure drop ΔP/Pa	Mean flow $Q/(10^{-13} \text{ m}^3 \cdot \text{s}^{-1})$	Flow resistance coefficient ξ
20	5.954	0.550	290345
25	3.534	0.971	103858
30	2.348	1.510	37128

From Tab. 2, it can be seen that as the inner diameter increases, the pressure drop and the flow resistance coefficient decrease while the mean flow increases. When the inner diameter is increased to 30 μm, the pressure drop reduces by approximately 60.56% and the flow resistance coefficient reduces by approximately 87.21%. This is mainly because the flow area in the vessel increases as the inner diameter increases, resulting in an increase in the mean flow which greatly decreases the pressure drop.

3.1.2 Influence of the Pitted Thickening Height

For this simulation, the pitted thickening patterns have dimensions of w = 2.3 μm, d = 30 μm, s = 4 μm, n = 4 and the axial rotation is 45°. The pitted thickening height is varied from 2.3 μm to 4 μm. Tab. 3 shows the influence of the pitted thickening height on the pressure drop and the flow resistance coefficient.

Table 3: Effect of pitted thickening height on pressure drop and flow resistance coefficient

Inner diameter of vessel/μm	Pressure drop ΔP/Pa	Mean flow $Q/(10^{-13} \text{ m}^3 \cdot \text{s}^{-1})$	Flow resistance coefficient ξ
2.3	2.348	1.510	37128
3.0	2.600	1.347	60522
3.5	2.823	1.236	86452
4.0	3.065	1.130	122352

From Tab. 3, it can be seen that as the pitted thickening height increases, the pressure drop and the flow resistance coefficient increase while the mean flow decreases. When the pitted thickening height is increased to 4 μm, the pressure drop increases by approximately 30.54% and the flow resistance coefficient increases by approximately 229.54%. This is mainly because the flow area in the vessel increases due to a reduction in the inner diameter of the fluid domain as the pitted thickening height increases, resulting in an increase in the mean flow and a rapid increase in the pressure drop.

3.1.3 Influence of the Pitted Thickening Width

For this simulation, the dimensions of the pitted thickening patterns are h = 2.3 μm, d = 30 μm, s = 4 μm, n = 4 and the axial rotation is 45°. The pitted thickening width is varied from 2.3 μm to 5.0 μm. Tab. 4 shows the influence of the pitted thickening width on the pressure drop and the flow resistance coefficient.

Table 4: Effect of pitted thickening width on pressure drop and flow resistance coefficient

Pitted thickening width/μm	Pressure drop ΔP/Pa	Mean flow $Q/(10^{-13} \ \mathrm{m^3 \cdot s^{-1}})$	Flow resistance coefficient ξ
2.3	2.348	1.510	37128
3.0	2.350	1.510	37215
4.0	2.351	1.510	37259
5.0	2.352	1.510	37303

From Tab. 4, it can be seen that as the pitted thickening width increases, the pressure drop and the flow resistance coefficient increase while the mean flow stays constant. When the pitted thickening width is increased to 5 μm, the pressure drop increases by approximately 0.17%, and the flow resistance coefficient increases by approximately 0.47%. This is mainly because the smooth area in the vessel decreases as the pitted thickening width increases, resulting in an increase in the pressure drop and the flow resistance coefficient in the vessel.

3.1.4 Influence of the Pitted Thickening Spacing

For this simulation, the dimensions of the pitted thickening patterns are w = 2.3 μm, h = 2.3 μm, d = 30 μm, n = 4 and the axial rotation is 45°. The pitted thickening spacing is varied from 2.4 μm to 4.8 μm. Tab. 5 shows the influence of the pitted thickening spacing on the pressure drop and the flow resistance coefficient.

Table 5: Effect of pitted thickening spacing on pressure drop and flow resistance coefficient

Pitted thickening width/μm	Pressure drop ΔP/Pa	Mean flow $Q/(10^{-13} \ \mathrm{m^3 \cdot s^{-1}})$	Flow resistance coefficient ξ
2.4	2.369	1.510	38047
3.2	2.358	1.510	37565
4.0	2.348	1.510	37128
4.8	2.329	1.510	36296

From Tab. 5, it can be seen that as the pitted thickening spacing increases, the pressure drop and flow resistance coefficient decrease while the mean flow stays constant. When pitted thickening spacing is increased to 4.8 μm, the pressure drop decreases by approximately 1.69%, and the flow resistance coefficient decreases by approximately 4.60%. This is mainly because the number of pits in the same area

decreases as the pitted thickening spacing increases, resulting in an increase in the pressure drop and the flow resistance coefficient in the vessel.

3.1.5 Influence of the Number of Laps

For this simulation, the dimensions of the pitted thickening patterns are w = 2.3 μm, h = 2.3 μm, s = 4 μm, d = 30 μm and the axial rotation is 0°. The number of laps is varied from 4 to 8. Tab. 6 shows the influence of the number of laps on the pressure drop and the flow resistance coefficient.

Table 6: Effect of the number of laps on pressure drop and flow resistance coefficient

Number of laps	Pressure drop ΔP/Pa	Mean flow $Q/(10^{-13} \text{ m}^3 \cdot \text{s}^{-1})$	Flow resistance coefficient ξ
4	2.348	1.510	37128
6	2.327	1.510	36208
8	2.311	1.510	35508

From Tab. 6, it can be seen that as the number of laps increases, the pressure drop and the flow resistance coefficient decrease while the mean flow stays constant. When the number of laps is increased to 8, the pressure drop decreases by approximately 1.45%, and the flow resistance coefficient decreases by approximately 4.02%. This is mainly because the equivalent radius of the vessel increases as the number of laps increases, so the pressure drop in the vessel increases and the flow resistance coefficient decreases. This also explains the reason for the large number of pits in the vessel.

3.1.6 Influence of the Adjacent Pit Axial Rotation

For this simulation, the dimensions of the pitted thickening patterns are w = 2.3 μm, h = 2.3 μm, s = 4 μm, n = 4 and d = 30 μm. The adjacent pit axial rotation is varied from 0° to 45°. Tab. 7 shows the influence of the adjacent pit axial rotation on the pressure drop and the flow resistance coefficient.

From Tab. 7, it can be seen that as the adjacent pit axial rotation increases, the pressure drop and the flow resistance coefficient firstly decrease and then increase while the mean flow stays constant. When the pressure drop is at its maximum, the adjacent pit axial rotation θ is 30° and the pressure drop has increased by approximately 0.34%, and the flow resistance coefficient increases by approximately 0.95%. This is mainly because the disturbance effect firstly decreases and then increases as the adjacent pit axial rotation increases, so the maximum pressure drop and flow resistance coefficient values occur at 30°.

Table 7: Effect of adjacent pit axial rotation on pressure drop and flow resistance coefficient

Adjacent pit axial rotation	Pressure drop ΔP/Pa	Mean flow $Q/(10^{-13} \text{ m}^3 \cdot \text{s}^{-1})$	Flow resistance coefficient ξ
axial rotation 0°	2.345	1.510	36996
axial rotation 15°	2.341	1.510	36821
axial rotation 30°	2.349	1.510	37171
axial rotation 45°	2.348	1.510	37128

3.2 Analysis of Flow Characteristics of Pitted Thickening

A pitted thickening vessel was selected to analyze the flow characteristics. For this model, the dimensions of the pitted thickening patterns are w = 2.3 μm, h = 2.3 μm, s = 4.8 μm, n = 4, d = 30 μm and the axial rotation is 45°. It can be seen from Fig. 6 that the pressure at the inlet wall is large, and the

pressure uniformly reduces with fluid flow. When a convex portion is encountered on a nearby wall surface, the local energy loss increases due to encountering resistance to the flow, and a pressure difference occurs before and after the convex portion. Fig. 7 shows that the overall flow velocity of the fluid along the vessel wall surface is very small. Due to the existence of pitted thickening, a local low velocity vortex flow is produced on the convex wall surface, causing the effective inner diameter to be smaller than the actual inner diameter of the vessel.
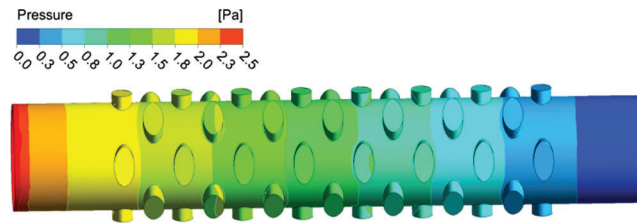

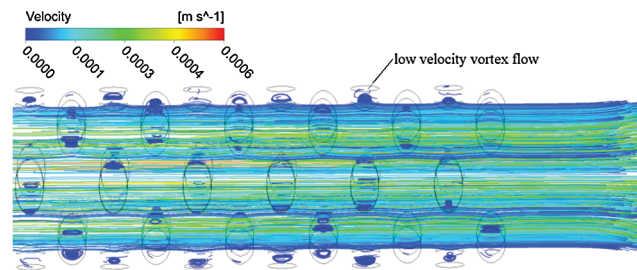**Figure 6:** Pressure distribution of fluid in a reticulated thickened vessel

Figure 7: Schematic of fluid flow along the wall of a vessel

3.3 Analysis of Resistance between Different Vessel Wall Thickening Patterns and Smooth Vessels

The different vessel wall thickening patterns and smooth vessels were compared and analyzed in order to study the water transport efficiency of a xylem vessel. The structural flow resistance of different thickened structures is calculated using:

$$F = (\xi - \xi_s)/\xi \tag{10}$$

where F is the structural flow resistance, ξ is the flow resistance coefficient for different vessel wall thickening patterns and ξ_s is smooth vessel flow resistance coefficient. It is obvious that the closer the structural flow resistance value is to 1, the closer the transmission efficiency of the wall thickening pattern is to an ideal vessel.

For this simulation, the three different thickening patterns have a flow region length of 150 μm and w = 2.3 μm, h = 2.3 μm and s = 4 μm. The resulting vessel pressure drops are shown in Tab. 8, which shows that the helical thickening and the annular thickening have a larger mean flow than the pitted thickening for the same inner diameter, since the pitted thickening has the largest area which means that the overall flow of the flow path is decreased.

The flow resistance coefficient of the different vessel thickening structures are shown in Tab. 9 and are obtained using Eq. (9). The relationship between the inner diameter and the structural flow resistance is calculated using Eq. (10), as shown in Fig. 8.
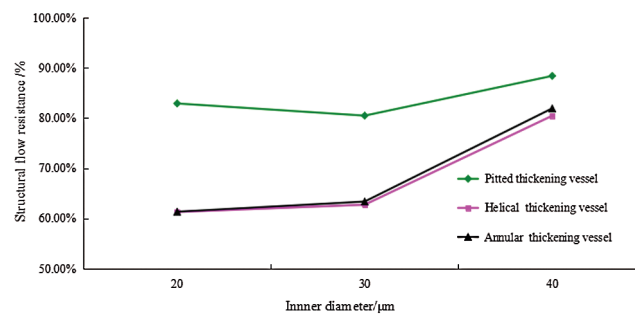
As shown in Fig. 8, the calculations show that the structural flow resistance of different wall thickening patterns is proportional to the size of the inner diameter of the vessel. Comparing the three types of wall

Table 8: Calculation of pressure drop of vessels with different thickening structures and smooth vessels

Inner Diameter of vessel D/µm	Helical thickening vessel pressure drop ΔP/ Pa	Annular thickening vessel pressure drop ΔP/ Pa	Smooth vessel pressure drop ΔP/ Pa	Mean flow Q/ (10^{-13} m^3·s^{-1})
20 µm	7.162	7.169	3.692	0.933
25 µm	3.920	3.962	2.403	1.463
30 µm	2.484	2.562	1.692	2.109

Table 9: Flow resistance coefficient of different vessel thickening structures

Inner Diameter of vessel D/µm	Pitted thickening vessel flow resistance coefficient ξ	Helical thickening vessel flow resistance coefficient ξ	Annular thickening vessel flow resistance coefficient ξ	Smooth vessel flow resistance coefficient ξ
20 µm	290345	128261	128419	49655
25 µm	103858	54432	55377	20288
30 µm	37128	22045	23836	4309

Figure 8: Relationship between structural flow resistance and inner diameter of different thickened vessel structures

thickening vessel structures, the pitted thickening vessel has the largest structural flow resistance, the annular thickening vessel has the second largest resistance and the helical thickening catheter has the smallest structural flow resistance. This indicates that the pitted thickening vessel is closest to the ideal vessel, which also explains the evolution of the wall thickening. As the inner diameter of the vessel increases, the structural flow resistance increases for all three types of wall thickening structures. This confirms the conclusions drawn by Tyree [2] and Chen [16] who observed that a vessel with a larger inner diameter would have a water transport efficiency that is much closer to an ideal vessel, since changes to the structural features of a vessel has less effect when the size of the vessel is large.

4 Conclusions

1. The flow resistance coefficient and the pressure drop were both found to be proportional to the thickening height, and thickening width, and inversely proportional to the inner diameter, thickening spacing and number of laps.
2. As the inner diameter was increased, the pressure drop reduced by approximately 60.56% and the flow resistance coefficient reduced by approximately 87.21%. As the pitted thickening height was increased, the pressure drop increased by approximately 30.54% and flow resistance coefficient

increased by approximately 229.54%. As the pitted thickening width was increased, the pressure drop increased by approximately 0.17% and the flow resistance coefficient increased by approximately 0.47%. As the pitted thickening spacing was increased, the pressure drop decreased by approximately 1.69% and the flow resistance coefficient decreased by approximately 4.60%. As the number of laps was increased, the pressure drop decreased by approximately 1.45% and the flow resistance coefficient decreased by approximately 4.02%. The maximum pressure drop occurred when the adjacent pit axial rotation was 30° and the pressure drop increased by approximately 0.34% and the flow resistance coefficient increased by approximately 0.95%.

3. The structural flow resistance is an indicator of the water transmission efficiency i.e., the closer the structural flow resistance is to 1, the closer the transmission efficiency of the wall thickening pattern is to an ideal vessel. The pitted thickening vessel has the largest structural flow resistance, which indicates that the pitted thickening vessel is closer to an ideal vessel and the structural flow resistance of the wall thickening is proportional to the inner diameter of the vessel.

Conflicts of Interest: The authors declare that they have no conflicts of interest to report regarding the present study.

References

1. Bai, D. Z., Deng, X. P., Huang, M. L. (2003). Water transportation and regulation in plants. *Acta Botanica Boreali-Occidentalia Sinica, 23(9),* 1637–1643.

2. Tyree, M. T., Zimmermann, M. H. (2002). *Xylem structure and the ascent of sap*. Berlin Heidelberg: Springer.

3. Lucas, W. J., Groover, A., Lichtenberger, R., Furuta, K., Yadav, S. et al. (2013). The plant vascular system: evolution, development and functions. *Journal of Integrative Plant Biology, 55(4),* 294–388. DOI 10.1111/jipb.12041.

4. Wan, X. C., Meng, P. (2007). Physiological and ecological mechanisms of long-distance water transport in plants: a review of recent issues. *Chinese Journal of Plant Ecology, 31(5),* 804–813. DOI 10.17521/cjpe.2007.0102.

5. Xiao, Y. J., Guo, C. Y., Chen, T., Xue, J. W. (2010). Primary analysis of plant water transportation model. *Chinese Journal of Applied Mechanic, 27(4),* 751–754.

6. Ellerby, D. J., Ennos, A. R. (1998). Resistances to fluid flow of model xylem vessels with simple and scalariform perforation plates. *Journal of Experimental Botany, 49(323),* 979–985. DOI 10.1093/jxb/49.323.979.

7. Kizilova, N. (2008). Long-distance liquid transport in plants. *Proceedings of the National Academy of Sciences of the United States of America, 57(3),* 179–203.

8. Han, Y. D., Chen, D. W., Liu, S. Q., Xu, G. (2020). An investigation into the effects of the Reynolds number on high-speed trains using a low temperature wind tunnel test facility. *Fluid Dynamics & Materials Processing, 16(1),* 1–19. DOI 10.32604/fdmp.2020.06525.

9. Roth, A. (1996). Water transport in xylem conduits with ring thickenings. *Plant, Cell and Environment, 19(5),* 622–629. DOI 10.1111/j.1365-3040.1996.tb00397.x.

10. Schulte, P. J. (1999). Water flow through a 20-pore perforation plate in vessels of *Liquidambar styraciflua*. *Journal of Experimental Botany, 50(336),* 1179–1187. DOI 10.1093/jxb/50.336.1179.

11. Ai, Q. L., Xu, F., Chen, Q., Chen, J., Wang, P. (2011). Flow resistance characteristics of scalariform perforation plates in plant xylem vessels. *Transactions of the Chinese Society for Agricultural Machinery, 42(8),* 143–148.

12. Karam, G. N. (2005). Biomechanical model of the xylem vessels in vascular plants. *Annals of Botany, 95(7),* 1179–1186. DOI 10.1093/aob/mci130.

13. Wooding, F. B. P., Northcote, D. H. (1964). The development of the secondary wall of the xylem in *Acer pseudoplatanus*. *Journal of Cell Biology, 23(2),* 327–337. DOI 10.1083/jcb.23.2.327.

14. Bierhorst, D. W., Zamora, P. M. (1965). Primary xylem elements and element associations of Angiosperms. *American Journal of Botany, 52(7),* 657–710. DOI 10.1002/j.1537-2197.1965.tb07236.x.

15. Carlquist, S. (2012). How wood evolves: a new synthesis. *Botany, 90(10),* 901–940. DOI 10.1139/b2012-048.

16. Chen, Q., Xu, F., Ai, Q. L., Zhang, L. B. (2015). Hydrodynamic model and flow resistance characteristics of plant vessel wall thickenings. *Transactions of the Chinese Society of Agricultural Engineering, 31(19),* 1–8.

17. Luo, Y., Liu, W., Wang, L., Xie, W. (2016). Heat and mass transfer characteristics of leaf-vein-inspired microchannels with wall thickening patterns. *International Journal of Heat and Mass Transfer, 101,* 1273–1282. DOI 10.1016/j.ijheatmasstransfer.2016.05.120.

18. Rand, R. H. (1983). Fluid mechanics of green plants. *Annual Review of Fluid Mechanics, 15(1),* 29–45. DOI 10.1146/annurev.fl.15.010183.000333.

19. Jeje, A. A. (1985). Flow models of microcapillaries of living plants. *Physical Hydrodynamics, 115,* 15–26.

20. Datta, A., Sanyal, D., Das, A. K. (2016). Numerical investigation of heat transfer in microchannel using inclined longitudinal vortex generator. *Applied Thermal Engineering, 108,* 1008–1019. DOI 10.1016/j.applthermaleng.2016.07.165.

21. Ebrahimi, A., Roohi, E., Kheradmand, S. (2015). Numerical study of liquid flow and heat transfer in rectangular microchannel with longitudinal vortex generators. *Applied Thermal Engineering, 78,* 1576–1583. DOI 10.1016/j.applthermaleng.2014.12.006.

22. Schulte, P. J. (2012). Computational fluid dynamics models of conifer bordered pits show how pit structure affects flow. *New Phytologist, 193(3),* 721–729. DOI 10.1111/j.1469-8137.2011.03986.x.

23. Nouri, S., Abderrahmane, G., Said, A., Pierre, S. (2018). A numerical study of the transitions of laminar natural flows in a square cavity. *Fluid Dynamics & Materials Processing, 14(2),* 121–135.

24. Cherfi, R., Sadaoui, D., Sahi, A., Mouloud, S. (2019). Numerical simulation of double diffusive mixed convection in a horizontal annulus with finned inner cylinder. *Fluid Dynamics & Materials Processing, 15(2),* 153–169. DOI 10.32604/fdmp.2019.04294.